Research Article

Songning Li, Peisheng Han, Yulin Xing, Yunlong Zhu, and Xiaogang Wang*

Study on the rheological behavior and microstructure evolution of isothermal compression of high-chromium cast steel

https://doi.org/10.1515/htmp-2025-0093
received March 09, 2025; accepted September 29, 2025

Abstract: This research elucidates the high-temperature deformation mechanisms in high-chromium cast steel through integrated constitutive analysis and microstructural characterization across thermomechanical processing conditions (1,150–1,250°C, 0.001–0.1 s^{-1}). The developed strain-compensated Arrhenius-type constitutive equation exhibits remarkable predictive capability for flow behavior, with deformation activation energy displaying fourth-order polynomial correlation with true strain. Processing map methodology identifies a stable processing domain (1,190–1,240°C, 0.001–0.005 s^{-1}) characterized by maximum energy dissipation efficiency. Electron backscatter diffraction analysis demonstrates that under optimal deformation parameters (1,200°C, 0.001 s^{-1}), high-chromium cast steel yields a fine-grained microstructure with 92.2% recrystallization fraction. Additionally, discontinuous dynamic recrystallization nucleation predominantly occurs via subgrain merging and boundary protrusion mechanisms.

Keywords: high chromium cast steel, constitutive model, processing map, dynamic recrystallization, texture

1 Introduction

With excellent strength, high-temperature oxidation resistance and corrosion resistance, high-chromium cast steel is widely applied to energy development, power machinery, petrochemicals, the power industry, aerospace, and other fields [1–4]. However, grain inhomogeneity and micro- and macro-segregation in high-chromium cast steel materials may result in fractures and abrasive wear of components during service, thereby limiting their broader industrial applications. It was reported that 638 safety accidents occurred in China's coal mining sectors between 2018 and 2022, and those caused by material component failures cost hundreds of millions of dollars in total [5,6]. In this study, significant improvement in the material properties of high-chromium cast steel is realized by establishing an accurate ontological model and determining the hot processing process window. Based on the dynamic recrystallization (DRX) critical conditions, optimizing the process parameters of large-scale high-chromium cast steel roll forging [7], plate rolling [8], and continuous casting billet hot delivery, reduces the production cost of major equipment parts and components, and improves the service life of the material; in the future, combined with advanced science and technology and intelligent manufacturing methods, building a systematic database of the material process can realize the virtual process design [9,10], and promote the high-chromium cast steel in the industrial field of high performance and intelligent development. Given these considerations, analyzing the hot deformation mechanisms and microstructural changes in high-chromium cast steel becomes imperative for industrial quality improvement.

True stress–strain curves have been utilized to assess the flow stress evolution in materials during hot deformation under varying processing conditions. Ye et al. [11] observed that the flow stress of 06Cr23Ni13 stainless steel was correlated negatively with the deformation temperature and positively with the strain rate, with an activation energy (Q) of 45.381 kJ·mol^{-1} during thermal deformation. Based on this finding, Chen et al. [12] developed a dual-corrected Arrhenius constitutive model that combined friction with temperature rise effects for accurate description of the flow stress evolution of α and β phases in TC18 titanium alloys. A high correlation coefficient (R = 0.98982) was observed between predicted and experimental values. Park et al. [13] determined the Johnson-Cook (J-C) constitutive

* **Corresponding author: Xiaogang Wang**, High-end Heavy Machinery and Equipment Research Institute, National Key Laboratory of Advanced Stainless Steel, Taiyuan University of Science and Technology, Taiyuan, 030024, China, e-mail: wxg@tyust.edu.cn
Songning Li, **Peisheng Han**, **Yulin Xing**, **Yunlong Zhu:** High-end Heavy Machinery and Equipment Research Institute, National Key Laboratory of Advanced Stainless Steel, Taiyuan University of Science and Technology, Taiyuan, 030024, China

equation for Inconel 601 through high-temperature tensile tests and verified its reliability. To systematically interpret deformation mechanisms during hot processing, Parsad et al. [14] pioneered the development of processing maps in 1984 and established fundamental criteria for plastic instability. Sun et al. [15] created thermal processing maps for identifying optimal processing parameters for 6A02 aluminum alloys. Wang et al. [16] evaluated the workability of Cu–Ag alloys by using processing maps to delineate safe processing zones and instability boundaries. Decades of experimental investigations have demonstrated the reliability of Parsad's criterion for assessing hot working mechanisms and microstructural transformations in metallic materials and composites, including stainless steel and superalloy systems.

The operative DRX regime during metal thermal processing critically controls the evolution of grain structure and consequent material properties. The new grains of low-layer misfit energy metals will grow and nucleate at the dislocation aggregation during thermal deformation, which is a typical phenomenon of discontinuous dynamic recrystallization (DDRX), whereas high-layer misfit energy materials first produce low-angle grain boundaries (LAGB) such as subcrystalline, and gradually transform into high-angle grain boundaries (HAGB) as thermal deformation continues to occur, a process known as continuous dynamic recrystallization (CDRX) [17]. Cizek's [18] work on duplex stainless steel systems demonstrated the co-existence of CDRX and DDRX phenomena, establishing that their mutual transformation is processing-history-dependent and microstructure-sensitive. Researchers have combined strain rate and deformation temperature into a single Zener–Hollomon parameter to facilitate the study of the DRX behavior of materials, Galiyev et al. [19] found that the DRX mechanism varies with the Z parameter, ZK60 Mg alloy's CDRX occurs mainly in the intermediate temperature range (473–523 K), while the DDRX mainly occurs above 573 K. In addition, the internal subcrystalline size and dislocation density of the material also affect the occurrence of DRX to some extent, which needs to be further verified with the help of advanced analytical techniques. With advancements in microstructural characterization techniques, electron backscatter diffraction (EBSD) has become indispensable for nanoscale analysis, particularly in quantifying dislocation slip systems and grain morphology to elucidate DRX behavior [20–22]. Saeidi et al. [23] employed EBSD to determine the nanoscale grain structure and crystallographic orientation distribution of severely deformed fine-grained DP780 steel. Li [24] et al. performed EBSD on aluminum alloys after hot rolling and found that the high strength of aluminum alloys is mainly due to the combined effect of strain hardening and fine grain strengthening. EBSD characterization was utilized by Liu et al. [25] to investigate the thermomechanical processing response and recrystallization kinetics in a Cu-based alloy containing Ti, Ni, and Si elements. The results revealed that Ni_3Ti precipitates promoted DRX and nucleation, and stabilized deformation zones, whereas Ni_2Si precipitates inhibited DRX and expanded instability regions.

The development of sophisticated characterization methods and improved detection capabilities has enabled remarkable advances in high-chromium cast steel research in recent years. Li et al. [26,27] investigated the microhardness evolution of high-chromium cast steel using laser cladding technology. It was found that austenite exhibited strong tempering stability, while the formation of ferrite was identified as the primary cause of hardness reduction. Researchers [28–31] have significantly enhanced the hardness and wear resistance of high-chromium cast steel by incorporating trace elements such as vanadium, niobium, chromium, and boron into the matrix. Recent studies have confirmed that precise control of thermomechanical processing variables significantly enhances the hot deformation behavior of engineering alloys. For instance, Li [32] successfully optimized the relationships between various variables to delineate the impact properties of 25CrMo4 steel under varying deformation conditions. Akbarzadeh [33] conducted a systematic study on the mechanism by which activation energy affects high-chromium tool steel. Despite these advancements, there is rare research that integrates flow stress models, processing maps, and microstructural characterization to comprehensively describe the hot workability of high-chromium cast steel at near-melting-point temperatures. This study systematically examines the hot deformation characteristics and microstructural changes in high-chromium cast steel. Through analysis of rheological behavior during hot compression tests (1,150–1,250°C), a constitutive model was developed from true stress–strain data, complemented by processing maps identifying optimal and unstable deformation regimes. Furthermore, EBSD orientation mapping revealed the relationship between grain structure and various variables. The conclusions of the study help to optimize the process parameters of hot rolling, forging, extrusion, etc., and improve the homogeneity and structural stability of the material. It provides theoretical guidance and technical paths for designing high-chromium alloys with high hardness, toughness, and fatigue resistance, promotes the research and development of a new generation of high-performance cast steel materials, and meets the demand for high-performance materials in the mining, construction, and machinery manufacturing industries. At the same time, it significantly improves national industrial

autonomy and realizes new breakthroughs in the field of high-performance wear-resistant materials.

2 Test materials and methods

The detailed chemical composition of the materials studied is shown in Table 1. The dimensions of the test specimens are as follows: Φ8 mm × 10 mm [34].

Thermal compression tests for high-chromium cast steel were performed using a Gleeble-3800 thermal simulator, and Figure 1 provides the schematic diagram. The specimen was heated to 1,250°C at 10°C·s^{-1} with 30 s stabilization, and subsequently cooled to target temperatures (1,150–1,250°C) at 5°C·s^{-1}, with a holding time of 60 s at each temperature. Axial compression tests were conducted at varying strain rates (0.001–0.1 s^{-1}), with a total deformation of 35%, followed by air cooling.

After thermal compression tests, the resulting true stress–strain data were generated to analyze the high-temperature flow behavior and evaluate the deformation characteristics of high-chromium cast steel under high-temperature conditions. Sample preparation involved axial sectioning and multi-step grinding to ensure surface quality for subsequent analysis, and etched with an alcoholic $FeCl_3$ solution to produce metallographic specimens. The micro-structure of the specimen was observed under a Keyence VHX-3000 ultra-depth-of-field metallographic microscope, and phase analysis were characterized using X-ray diffraction (XRD). Following electrochemical etching with a 10% perchloric acid/90% ethanol solution (20 V, 1 A), microstructural characterization was performed using EBSD equipment.

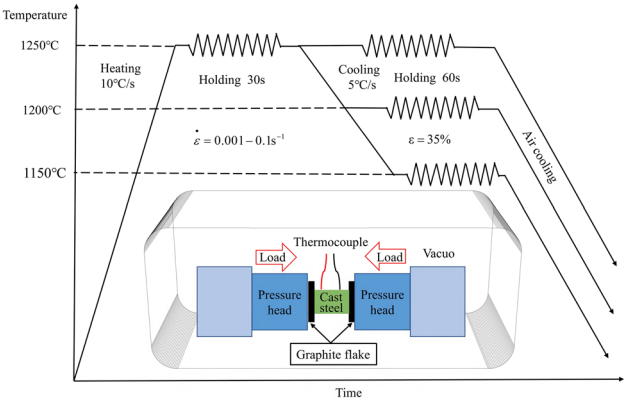

Figure 1: Schematic diagram of thermal compression of high chromium cast steel.

3 Results and discussion

3.1 True stress–true strain curve

Figure 2(a)–(c) presents the true stress–strain behavior of high-chromium cast steel across different thermomechanical conditions. The deformation process exhibits three characteristic regimes: Initial deformation showed linear work-hardening behavior, where rising dislocation density with increasing strain caused proportional flow stress enhancement. Next stage, the material response transitioned to a nonlinear hardening phase where flow stress continued rising with diminishing rates until attaining peak stress, corresponding to the threshold strain for microstructural instability. This peak stress occurred because the material began to soften dynamically internally once the true strain surpassed the critical strain for DRX. This phenomenon diminished the effects of work hardening, but work hardening remained the dominant mechanism. During the tertiary deformation stage, the flow stress attained a plateau regime where dynamic equilibrium was established between competing work-hardening and dynamic softening mechanisms, exhibiting characteristic steady-state deformation behavior with strain-independent flow stress.

Figure 2(d) demonstrates the evolution of peak stress during thermomechanical processing. The flow stress reaches its maximum value at a critical strain of 0.02, corresponding to the transition point between work-hardening and dynamic softening regimes. Under varying deformation conditions, the maximum flow stress is 58.749 MPa, while the minimum flow stress is 5.945 MPa. At a low strain rate ($\dot{\varepsilon}$ = 0.001 s^{-1}), the flow stress reaches its peak and then stays almost unchanged. Conversely, at high strain rates ($\dot{\varepsilon}$ = 0.01–0.1 s^{-1}), it achieves the maximum due to work hardening and then stabilizes after a brief decline. It indicates that dynamic softening significantly mitigated work hardening and became the dominant mechanism. In general, during the thermal compression deformation of high-chromium cast steel, the flow stress decreases with the temperature and increases with the strain rate, exhibiting typical negative temperature sensitivity and positive

Table 1: Chemical element content of the test material (wt%)

Element	C	Si	Mn	P	S	Mo	Ni	Cr	Fe
Content	0.051	0.32	0.53	0.012	0.003	1.45	5.03	26.1	Bal.

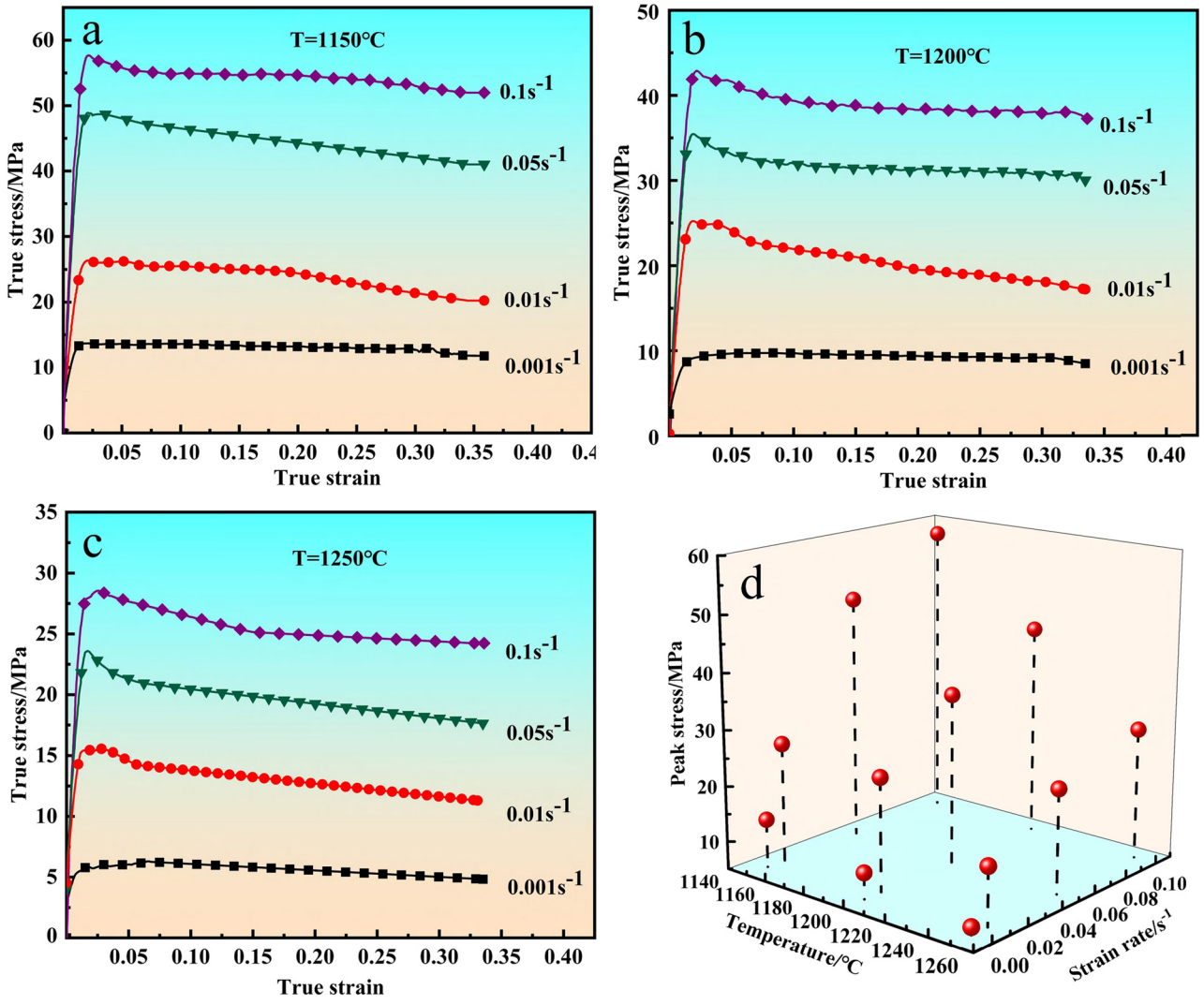

Figure 2: True stress–true strain curves of high chromium cast steel under different deformation conditions: (a) T = 1,150°C, (b) T = 1,200°C, (c) T = 1,250°C, and (d) peak stress diagram.

strain rate sensitivity [35]. The flow stress evolution is dictated by the competitive interplay between dislocation-mediated work hardening and thermally activated dynamic softening mechanisms. The specific mechanisms of dynamic softening require further confirmation through microstructural analysis.

3.2 Constitutive equation

Constitutive equations provide a theoretical foundation for establishing parameters related to material thermal processing. They predict the trends of the flow stress of materials and ensure that thermal processing equipment meets the load and energy requirements during material deformation, thereby improving thermal processing efficiency. In the present study, the Arrhenius constitutive model [36] was utilized to describe flow stress trends of high-chromium cast steel during the thermal compression deformation. The functional relationship among various variables are commonly described by the following equation:

$$\dot{\varepsilon} = A_1\sigma^{n_1}\exp\left(\frac{-Q}{RT}\right) \quad \alpha\sigma < 0.8, \tag{1}$$

$$\dot{\varepsilon} = A_2\sigma^{n_1}\exp(\beta\sigma)\exp\left(\frac{-Q}{RT}\right), \quad \alpha\sigma > 1.2, \tag{2}$$

$$\dot{\varepsilon} = A[\sinh(\alpha\sigma)]^n \exp\left(\frac{-Q}{RT}\right), \tag{3}$$

for all σ,here Q is the deformation activation energy (kJ·mol^{-1}); R = 8.314 kJ·mol^{-1}; A_1, A_2, A, n_1, β, n, and α all are constants, $\alpha = \beta/n_1$.

The Zener–Hollomon parameter [37] was utilized to characterize the effects of the deformation temperature and strain rate on thermal deformation behavior. The relationship between $\dot{\varepsilon}$ and T is described as:

$$Z = \dot{\varepsilon} \exp\left(\frac{Q}{RT}\right). \tag{4}$$

Eqs. (1)–(3) can be transformed into Eqs. (5)–(7)

$$\ln \dot{\varepsilon} = \ln A_1 + n_1 \ln \sigma - \frac{Q}{RT}, \tag{5}$$

$$\ln \dot{\varepsilon} = \ln A_2 + \beta\sigma - \frac{Q}{RT}, \tag{6}$$

$$\ln \dot{\varepsilon} = \ln A + n \ln[\sinh(\alpha\sigma)] - \frac{Q}{RT}. \tag{7}$$

Parameters n_1 and β were obtained as the respective slopes of the linear regressions in Figure 3(a) and (b) from Eqs. (5) and (6). The stress exponent n and apparent activation energy term Q/Rn were derived from the slopes of the Arrhenius plots in Figure 3(c) and (d) for ln[sinh($\alpha\sigma$)] vs ln$\dot{\varepsilon}$ and 1,000/T, respectively.

The values of the constants n_1, β, α, and n in the Arrhenius eigenstructure equation were obtained by describing the data fitting relationship, as shown in Table 2.

Figure 3(d) reveals an inverse relationship between strain rate and apparent activation energy (Q), where decreasing $\dot{\varepsilon}$ leads to higher Q values, because under low strain rate (0.001 s^{-1}), the DRX phenomenon is significant, and there is enough time for diffusion movement between

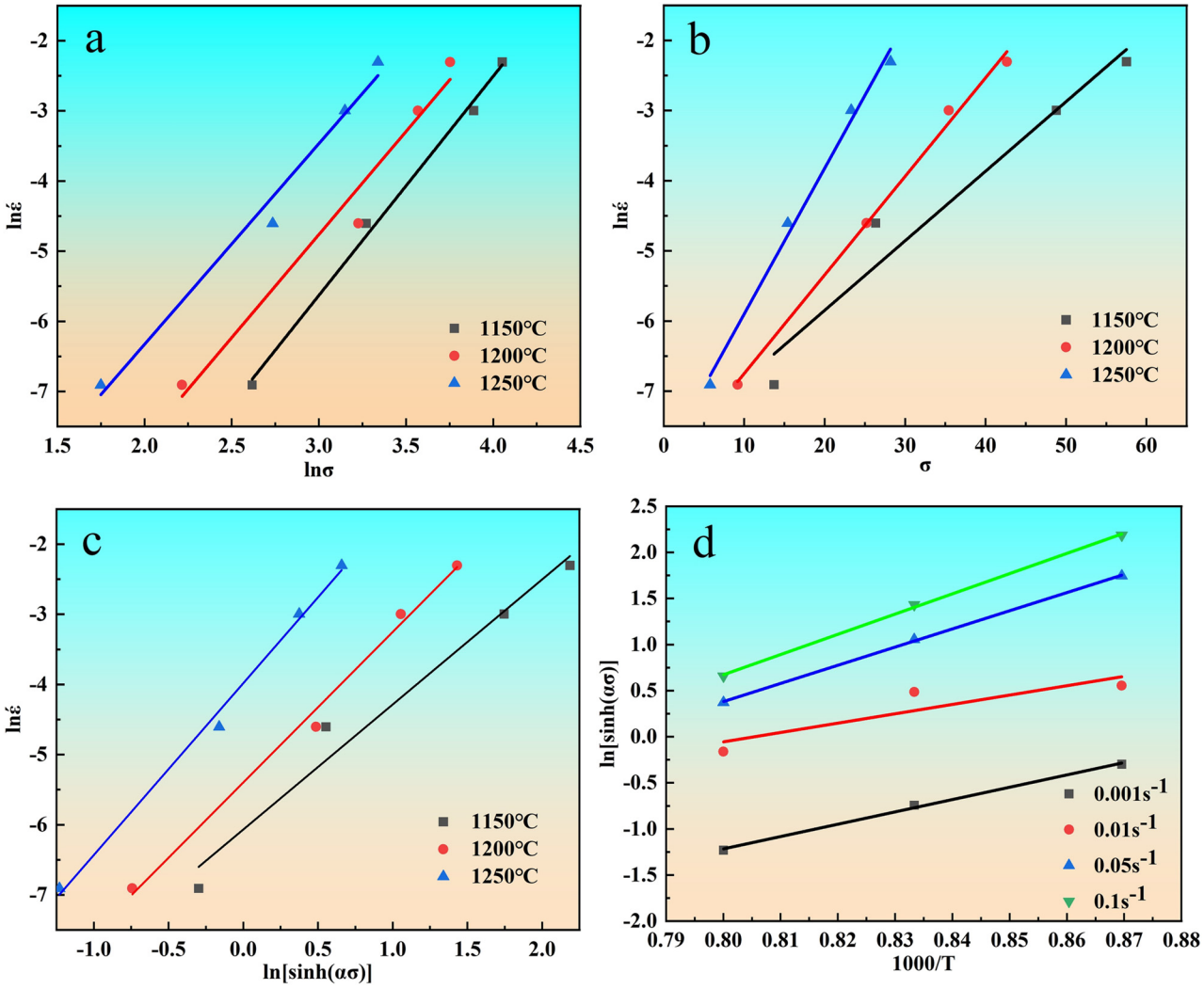

Figure 3: Fitting relationship of parameters (a) lnσ–lnε̇, (b) σ–lnε̇, (c) ln[sinh(ασ)]–lnε̇, and (d) ln[sinh(ασ)]–1,000/T.

Table 2: Values of fitting parameters n_1, β, α, n for different deformation conditions

Temperature (°C)	n_1	β	α	n
1,150	3.06117	0.21777	0.04998	2.16127
1,200	3.16037	0.14877	0.05312	2.29863
1,250	3.17041	0.10289	0.05499	1.84305

atoms, and the deformation activation energy is increased greatly. On the contrary, at a high strain rate (0.1 s^{-1}), the dislocation slip mechanism inside the material dominates and the deformation activation effect is weakened. Therefore, the deformation activation energy is typically negatively correlated with the strain rate.

Eqs. (3) and (4) can be transformed into the following:

$$\ln Z = \ln A + n \ln[\sinh(\alpha\sigma)]. \tag{8}$$

α, n, and Q were substituted in Eq. (8) and the values of ln$Z$ and ln[sinh($\alpha\sigma$)] were fitted (Figure 4), since the intercept is the value of lnA.

The strain dependence of constitutive parameters was rigorously modeled through quartic polynomial functions, the function demonstrated strong correlation and generalization abilities [38], as shown in the following equations:

$$\alpha = D_0 + D_1\varepsilon + D_2\varepsilon^2 + D_3\varepsilon^3 + D_4\varepsilon^4, \tag{9}$$

$$n = E_0 + E_1\varepsilon + E_2\varepsilon^2 + E_3\varepsilon^3 + E_4\varepsilon^4, \tag{10}$$

$$Q = F_0 + F_1\varepsilon + F_2\varepsilon^2 + F_3\varepsilon^3 + F_4\varepsilon^4, \tag{11}$$

$$\ln A = H_0 + H_1\varepsilon + H_2\varepsilon^2 + H_3\varepsilon^3 + H_4\varepsilon^4. \tag{12}$$

The material parameters of high-chromium cast steel were fitted into eigenequations and the quartic polynomial functions of strain were obtained. The results are presented in Table 3:

Table 3: Fitting parameters of material constants α, n, Q, and ln$A$

α	n	Q	ln$A$
D_0 = 0.05248	E_0 = 2.03541	F_0 = 334.35249	H_0 = 23.19775
D_1 = −0.13546	E_1 = 5.77662	F_1 = −1060.75539	H_1 = 20.71486
D_2 = 1.53978	E_2 = −43.5612	F_2 = 12232.8385	H_2 = 243.3865
D_3 = −5.68708	E_3 = 134.3812	F_3 = −45902.8302	H_3 = −1526.92
D_4 = 7.17332	E_4 = −157.588	F_4 = 53942.39428	H_4 = 2036.609

The Arrhenius flow stress equation for high-chromium cast steel under hot compression can be expressed as

$$\sigma = \frac{1}{\alpha}\ln\left\{\left(\frac{Z}{A}\right)^{\frac{1}{n}} + \left[\left(\frac{Z}{A}\right)^{\frac{2}{n}} + 1\right]^{\frac{1}{2}}\right\}. \tag{13}$$

Linear correlation coefficients R, Eq. (14) and average absolute relative errors (AARE, Eq. 15) were employed to assess the accuracy of the flow stress equations to predict the experimental true stress [12]. Experimental true stresses obtained at true strain of 0.35 were linearly fitted to predicted values, as shown in Figure 5.

$$R = \frac{\sum_{i=1}^{i=N}(\sigma_e^i - \bar{\sigma}_e)(\sigma_c^i - \bar{\sigma}_c)}{\sqrt{\sum_{i=1}^{i=N}(\sigma_e^i - \bar{\sigma}_e)^2 \sum_{i=1}^{i=N}(\sigma_c^i - \bar{\sigma}_c)^2}}, \tag{14}$$

$$\text{AARE} = \frac{1}{N}\sum_{i=1}^{i=N}\left|\frac{\sigma_e^i - \sigma_c^i}{\sigma_e^i}\right| \times 100\%, \tag{15}$$

where σ_e, σ_c, $\bar{\sigma}_e$, and $\bar{\sigma}_c$ represent experimental value, predicted value, and their respective averages.

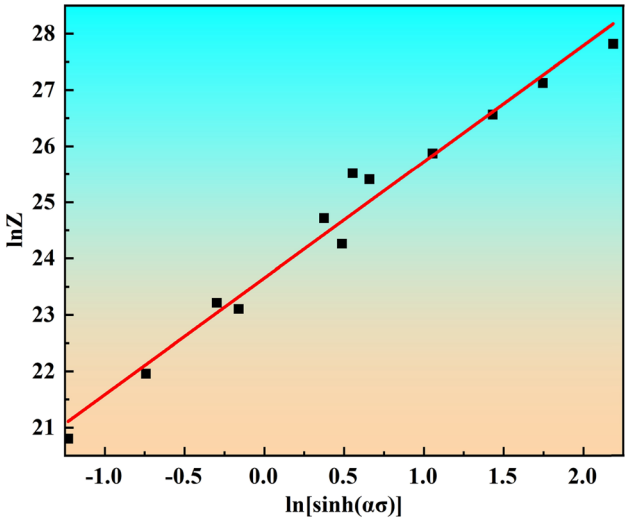

Figure 4: ln$Z$-ln[sinh($\alpha\sigma$)] numerical fitting relationship.

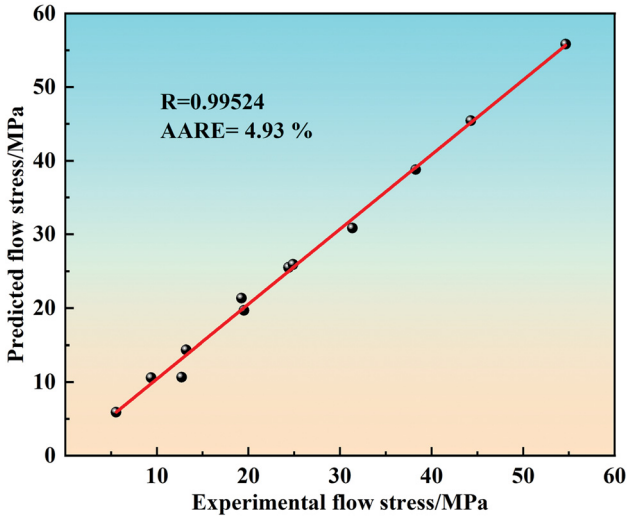

Figure 5: Correlation between experimental values and predicted values.

The Arrhenius-type constitutive model exhibited exceptional predictive accuracy, as evidenced by: R = 0.99524, and AARE = 4.93%. According to the correlation graph, excellent R and AARE value indicate that the flow stress equation derived from the Arrhenius constitutive equation can accurately predict the mechanical behavior of high-chromium cast steel during thermal compression deformation. This finding provides a theoretical foundation and practical insights for the industrial application of high-chromium cast steel.

3.3 Processing map

A thermal processing map can predict microstructural changes and determine the optimal grain size organization. It can accurately identify stable and destabilized deformation regions, reveal the microscopic deformation mechanisms in various regions, and help avoid destabilized regions while identifying the optimal thermal processing parameters. Utilizing a thermal processing map to describe the relationship between energy dissipation and microstructural evolution during material deformation effectively reduces the risk of fracture failures during thermal processing [15]. Based on the principles of dynamic materials modeling (DMM), the total energy dissipation rate during the thermal deformation of metals is divided into two components, G and J [14], which are expressed in the following equation:

$$P = \sigma\dot{\varepsilon} = G + J = \int_0^{\dot{\varepsilon}} \sigma d\dot{\varepsilon} + \int_0^{\sigma} \dot{\varepsilon} d\sigma, \tag{16}$$

where G and J represent the energy consumed, and m is introduced to describe the rate of change of both

$$m = \frac{\partial J}{\partial G} = \frac{\partial \ln \sigma}{\partial \ln \dot{\varepsilon}}. \tag{17}$$

Eq. (18) represents the flow stress under constant temperature and strain.

$$\sigma = K\dot{\varepsilon}^m. \tag{18}$$

The power J of energy consumed for microstructure evolution of high chromium cast steel is expressed as

$$J = \frac{m}{m+1}\sigma\dot{\varepsilon}. \tag{19}$$

The value range of m is $0 < m \le 1$, when $m = 1$ represents the power dissipation generated by the microstructure change, the maximum is reached. The power dissipation eficiency η can be defined as

$$\eta = \frac{J}{J_{\max}} = \frac{2m}{m+1}. \tag{20}$$

To evaluate the stability of materials in the thermal deformation process, Zieler investigated the irreversible thermodynamic principles of large plastic flow in continuum mechanics. Based on the DMM theory, an instability parameter (ξ) was introduced to establish a criterion for material instability during continuous thermal deformation [39]

$$\xi(\dot{\varepsilon}) = \frac{\partial \ln\left(\frac{m}{m+1}\right)}{\partial \ln \dot{\varepsilon}} + m \le 0. \tag{21}$$

Under constant strain rate and deformation temperature conditions, a cubic polynomial function was employed to fit and ensure the accuracy of the strain rate sensitivity index, (m)

$$\ln \sigma = a_0 + a_1(\ln \dot{\varepsilon}) + a_2(\ln \dot{\varepsilon})^2 + a_3(\ln \dot{\varepsilon})^3, \tag{22}$$

where a_0, a_1, a_2, a_3 are constants.

$$m = \left|\frac{\partial \ln \sigma}{\partial \ln \dot{\varepsilon}}\right|_{\dot{\varepsilon},T} = |3a_3(\ln \dot{\varepsilon})^2 a_0 + 2a_2(\ln \dot{\varepsilon}) + a_1|. \tag{23}$$

A two-dimensional plane is determined by T and ln$\dot{\varepsilon}$. The equivalent contour curve of η is drawn on the plane, and the power dissipation diagram of the material under corresponding conditions was obtained. By substituting Eq. (23) in (21) yields

$$\xi(\dot{\varepsilon}) = \frac{\partial \ln\left(\frac{m}{m+1}\right)}{\partial \ln \dot{\varepsilon}} + m = \frac{6a_3 \ln \dot{\varepsilon} + 2a_2}{m(m+1)} + m \le 0. \tag{24}$$

Within the interval defined by the deformation instability criterion and T-ln $\dot{\varepsilon}$, $\xi < 0$ represents the flow instability region. To ensure the rationality of the hot working process, process parameters must be carefully selected to avoid this region.

Figure 6 illustrates the three-dimensional power dissipation diagrams of high-chromium cast steel at strains of 0.05, 0.15, 0.25, and 0.35. Different colors represent variations in power dissipation values of the material during thermal deformation, and the magnitude of these values correlates to the microstructure evolution of the material [15]. The power dissipation map in Figure 6(a) reveals that η value is strongly temperature-strain rate dependent, where elevated thermal energy promotes microstructure evolution (higher η) whereas increased strain rate limits dynamic restoration processes (lower η). In region I, the power dissipation value ($\eta_{\max}$ = 0.57) is the maximum at a true strain of 0.05. Region II corresponds to lower power dissipation values of high-chromium cast steel during

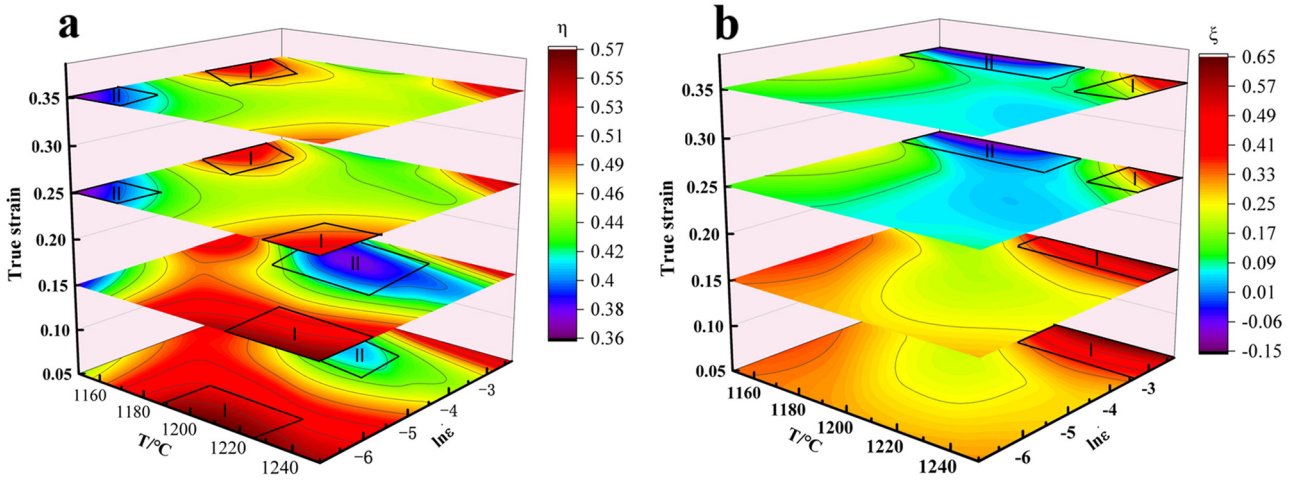

Figure 6: (a) Power dissipation diagram of high-chromium cast steel and (b) instability diagram of high-chromium cast steel.

thermal deformation, with a minimum value of η_{min} = 0.41 at a true strain of 0.05. The η_{max} value decreases to 0.52 while the η_{min} value in region II decreases to 0.36 as the true strain increases to 0.35. To mitigate the influence of wedge cracks [40] on power dissipation during thermal deformation, the material destabilization value (ξ) must be considered. Figure 6(b) presents the destabilization diagram of high-chromium cast steel under varying strain conditions. $\xi < 0$ and $\xi \geq 0$ represent the destabilization and safe processing zones, respectively. In region I, ξ exceeds 0 at a strain of 0.05 (ξ_{max} = 0.58), and no significant destabilization zone is observed. Region II (Figure 6b) exhibits flow instability characteristics when true strain exceeds 0.15, with pronounced manifestations occurring under low-temperature and high-strain conditions. Considering the patterns of power dissipation and material destabilization values, the destabilization region in the thermal deformation process of high-chromium cast steel gradually expands with the increasing true strain. Therefore, a larger true strain value should be selected for assessing material machinability.

A two-dimensional thermal processing map can be created for high-chromium cast steel by superimposing the power dissipation and flow instability diagrams under identical conditions [41]. This investigation established a two-dimensional processing map (ε = 0.35) to identify optimal thermomechanical processing windows for high-chromium cast steel. Figure 7 reveals distinct instability regimes (shaded areas) characterized by suboptimal power dissipation efficiency (η < 0.35), predominantly occurring within 1,150–1,190°C and 0.008–0.1 s^{-1} parameter range, suggesting limited dynamic restoration capability under these conditions. As deformation increases, the instability zone extends toward higher temperatures due to the suppression of the dynamic softening mechanism at lower temperatures. As a result, local flow at the junctions of large deformation regions becomes instable, leading to the formation of adiabatic shear zones and significant surface quality degradation. Thus, this instability zone is not applicable to thermal processing. The region (1,190–1,240°C, 0.001–0.005 s^{-1}) is the safe processing zone for the material. In this region, dynamic softening occur, consuming a significant amount of energy stored in the internal microstructure. The η value in this zone reaches up to 0.55, as indicated in the marked area A of the figure. It demonstrates excellent formability of the material within this processing interval. In summary, flow instability in the material is concentrated in low-temperature regimes (both high and low strain rates), while the safe processing zone predominantly covers high-temperature-low-strain-rate

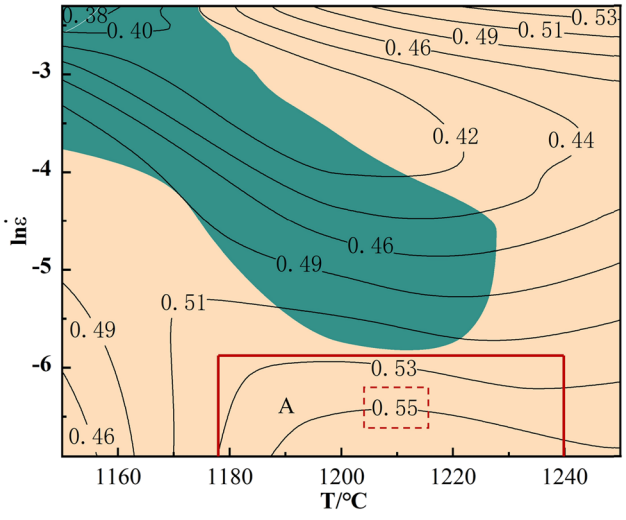

Figure 7: Two-dimensional processing map of high chromium cast steel showing the relationship between temperature and strain rate.

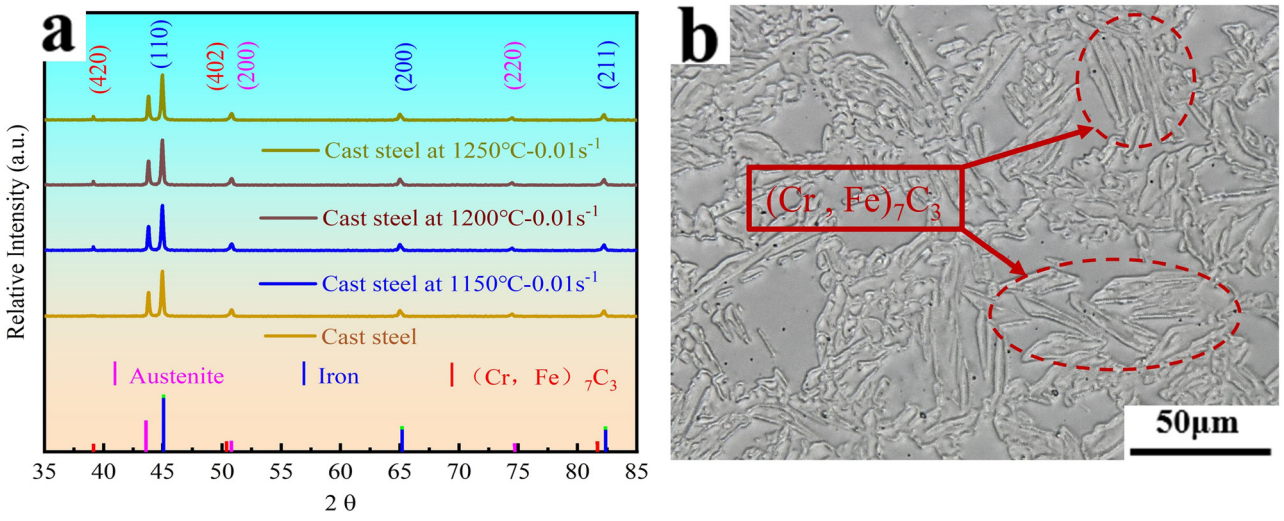

Figure 8: XRD diffraction pattern and microstructure of high-chromium cast steel under different deformation conditions: (a) XRD diffraction patterns at various temperatures and strain rate of 0.01 s^{-1}, (b) microstructure at 1,150°C, and strain rate of 0.01 s^{-1}.

scenarios, with limited high-strain-rate exceptions. This implies that strain rate has negligible control over the thermal processing behavior of high-chromium cast steel, whereas temperature sensitivity is markedly higher. The optimum deformation conditions are identified as 1,190–1,240°C and 0.001–0.005 s^{-1}.

3.4 Micro-organizational evolution

3.4.1 Microstructure of high-chromium cast steel

In order to analyze the phase composition characteristics of high-chromium cast steel under varying deformation conditions, XRD was conducted on the specimens, and the diffraction peaks were calibrated. As shown in Figure 8(b), the microstructure primarily consists of austenite and ferrite, exhibiting a tendency for grain refinement. A small amount of rod-like $(Cr,Fe)_7C_3$-type carbides [42] were observed at grain boundaries, forming a reticulated structure around grains. However, a small part of them existed as free particles. It indicates that the matrix structure of high-chromium cast steel underwent changes during the thermal deformation process. To investigate the microstructural evolution, EBSD was employed for detailed analysis.

3.4.2 Effect of deformation temperature on microstructure

To examine microstructural evolution in high-chromium cast steel under isostrain-rate (0.001 s^{-1}) and variable-temperature conditions, inverse pole figure (IPF), grain boundary (GB), and grain orientation spread (GOS) maps were systematically analyzed. Figure 9(a1)–(c1) reveal a progressive grain refinement with rising deformation temperatures, accompanied by pronounced morphological changes. At 1,150°C, grain sizes vary widely (3.47–87.52 μm), featuring predominantly deformation-oriented grains with sporadic fine grains from plastic strain. Inadequate thermal energy input at this stage restricts DRX, leaving deformed grains partially unreplaced. As temperature escalates to 1,250°C, the average grain size diminishes from 11.09 to 10.56 μm, reflecting enhanced energy input that accelerates DRX nucleation. Figure 9(d1) demonstrates a non-monotonic grain size trend, reaching a minimum (8.37 μm, 43% sub-average grains) at 1,200°C. This refinement stems from deformation-induced grain fragmentation and lattice distortion, where stored energy triggers thermodynamic instability. At 1,200°C, highly distorted zones preferentially nucleate polygonal DRX grains, progressively replacing the deformed grains.

Figure 9(a2)–(c2) present GB maps of high-chromium cast steel at a constant strain rate (0.001 s^{-1}) across varying temperatures. The microstructure is predominantly composed of HAGBs; (>15°, black lines), with minor fractions of medium-angle grain boundaries (MAGBs; 5–15°, blue lines) and LAGBs; (2–5°, red lines). As temperature increases from 1,150 to 1,250°C, the HAGB fraction exhibits a non-monotonic trend, reaching a maximum of 95.2% at 1,200°C. This peak HAGB concentration confirms DRX as the governing mechanism during thermal deformation. Beyond 1,200°C, Figure 9(d2) reveals increased LAGB and MAGB fractions, resulting from enhanced plastic

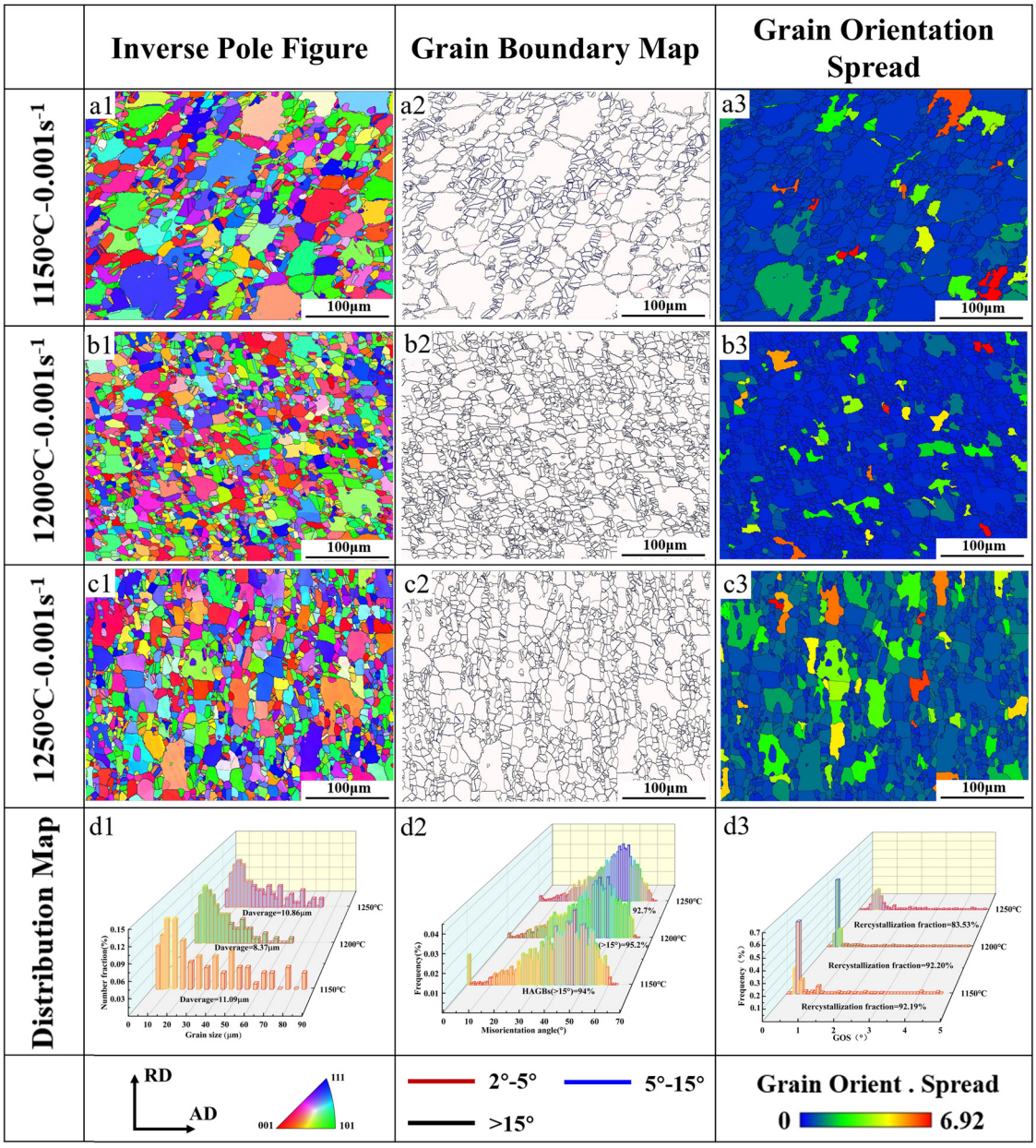

Figure 9: IPF maps, GB maps, and GOS maps of high chromium cast steel at a strain rate of 0.001 s^{-1} under different deformation temperatures: (a1–a3) microscopic images at 1150°C, (b1–b3) microscopic images at 1200°C, (c1–c3) microscopic images at 1250°C, (d1–d3) average grain size distribution diagrams, high-angle grain boundary distribution diagrams and recrystallization distribution diagrams at 1150°C–1250°C.

deformation at elevated temperatures. This promotes slip and twinning band formation within grains, followed by energy-driven generation of fine, randomly dispersed grain boundaries adjacent to recrystallized regions.

Figure 9(a3)–(c3) display (GOS) distributions at a constant strain rate (0.001 s^{-1}) across different deformation temperatures. Recrystallized (indicated by blue) and deformed grains (indicated by red) are identified by GOS values below and above 2°, respectively. With the increase in temperature from 1,150 to 1,200°C, the peak GOS value in the deformation region decreases from 6.02 to 5.11, and the deformation region gradually diminishes. This trend indicates a lower strain gradient and a more uniform strain distribution in high-chromium cast steel during thermal deformation. Deformed grains were surrounded by recrystallized ones, thereby minimizing the likelihood of significant deformation. At a deformation temperature of 1,250°C, the strain gradient in the red region increases significantly, compared with that in the blue region. It indicates greater lattice distortion and a higher propensity for plastic

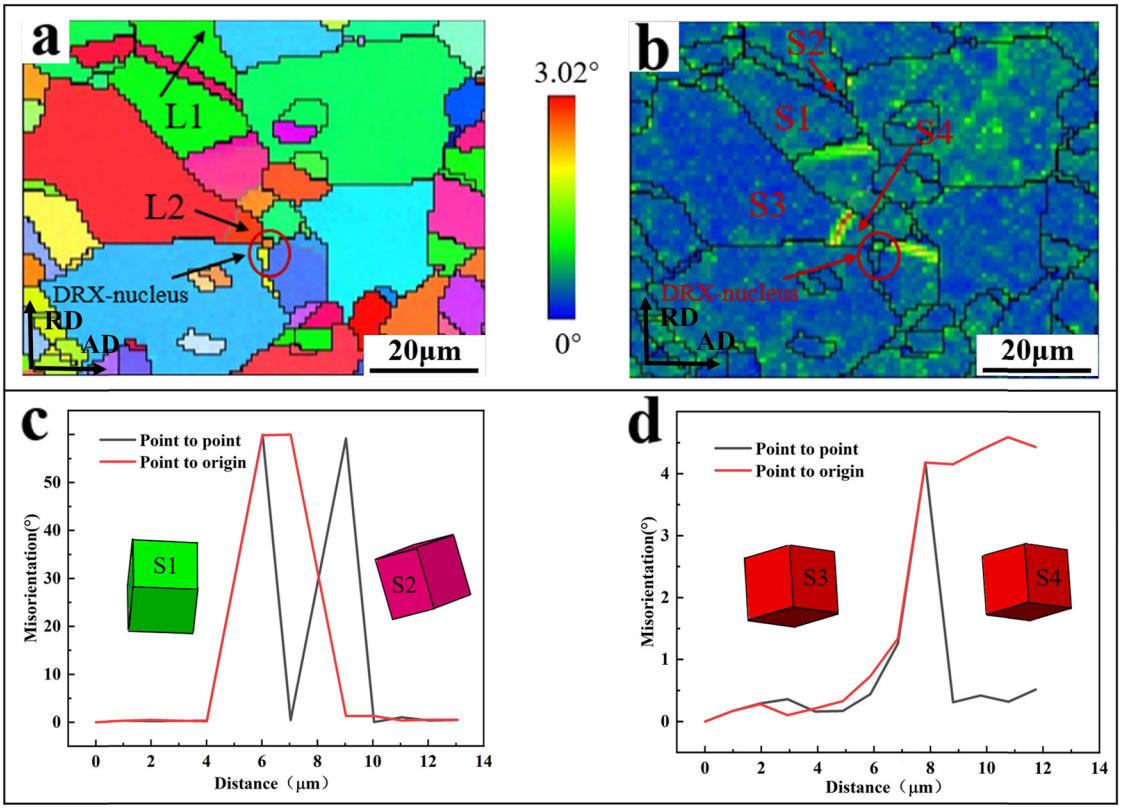

Figure 10: Local magnification of microscopic grains of high-chromium cast steel at 1,200°C and strain rate of 0.001 s^{-1}: (a) IPF image, (b) Geometrically necessary dislocation (GND) distribution image, (c) distribution of grain orientation difference along L1 direction, and (d) distribution of grain orientation difference along L2 direction.

deformation. As shown in Figure 9(d3), the recrystallization rate increases to a maximum of 92.20% at 1,200°C, suggesting that sufficient DRX occurred within the material at this temperature. When the deformation temperature exceeds 1,200°C, the recrystallization rate gradually decreases due to the significant increase in plastic deformation during thermal processing.

Figure 10 illustrates the local magnification of high-chromium cast steel at 1,200°C and 0.001 s^{-1}. Figure 10(a) shows that elongated S2 grains traverse the S1 matrix and extend to form independent grains. To determine the orientation relationship between the two grains, line L1 is drawn across the entire S2 grain starting from S1. Figure 10(c), cubic crystals represent the orientation of individual grains, with Euler angles of (174.3°, 43.8°, 4.4°) for S1 and (289.6°, 42.8°, 86.1°) for S2. The cumulative orientation difference between S1 and S2 reaches 60°, indicating that S2 was formed from S1 through multi-angle rotations and offsets during deformation. It is prevalent that smaller grains cross through larger ones, as deformation increased the dislocation density between initially randomly distributed grains, enhancing interaction forces and hindering dislocation slip. Consequently, intergranular elongated twins developed as a strain accommodation mechanism to mitigate the accumulated deformation. As shown in Figure 10(b), a distinct LAGB is formed between S3 and S4 grains. Line L2 is drawn from S3 to S4, crossing the GB of both grains. The Euler angle analysis reveals near-identical crystallographic orientations for grains S3 (261.7°, 45.7°, 17.6°) and S4 (261.2°, 46.0°, 18.2°), as illustrated in Figure 10(d). The calculated misorientation angle of 4° between these adjacent grains confirms the presence of an LAGB, consistent with the expected angular deviation range (2°–5°) for such boundaries. It indicates that fine subgrains were generated within original grains during thermal deformation, and they absorbed energy in regions of high dislocation density, rotated, and merged, eventually transforming from LAGBs and MAGBs into HAGBs. This phenomenon is called CDRX [43]. Additionally, numerous recrystallization nucleation points are observed at HAGBs (highlighted by red circles in the figure). The disordered atomic configuration at grain boundaries facilitates substantial misorientation energy storage, creating favorable nucleation sites for recrystallization. High-chromium cast steel demonstrates pronounced thermal sensitivity, where elevated deformation temperatures enhance

dynamic softening effects and reduce peak flow stress. Microstructural evolution during thermal processing follows a characteristic trend: average grain size, HAGB fraction, and recrystallization rate all exhibit non-monotonic temperature dependence, initially decreasing before increasing. This behavior stems from competing mechanisms-higher temperatures promote localized plastic deformation. Optimal processing conditions (1,200°C–0.001 s^{-1}) yield exceptional grain refinement (8.37 μm average size) and near-complete recrystallization (92.20%), demonstrating the material's processing window.

3.4.3 Effect of strain rate on microstructure

The strain rate dependence of microstructural evolution in high-chromium cast steel was systematically investigated under isothermal conditions (1,200°C). As revealed by IPF maps and grain size distributions (Figure 11(a1)–(d1)), increasing the strain rate from 0.01 s^{-1} to 0.1 s^{-1} promoted grain refinement, reducing the average grain size by 13.2% (from 8.43 to 7.32 μm). This microstructural trend correlates directly with the mechanical response observed in true stress–strain curves, where elevated strain rates

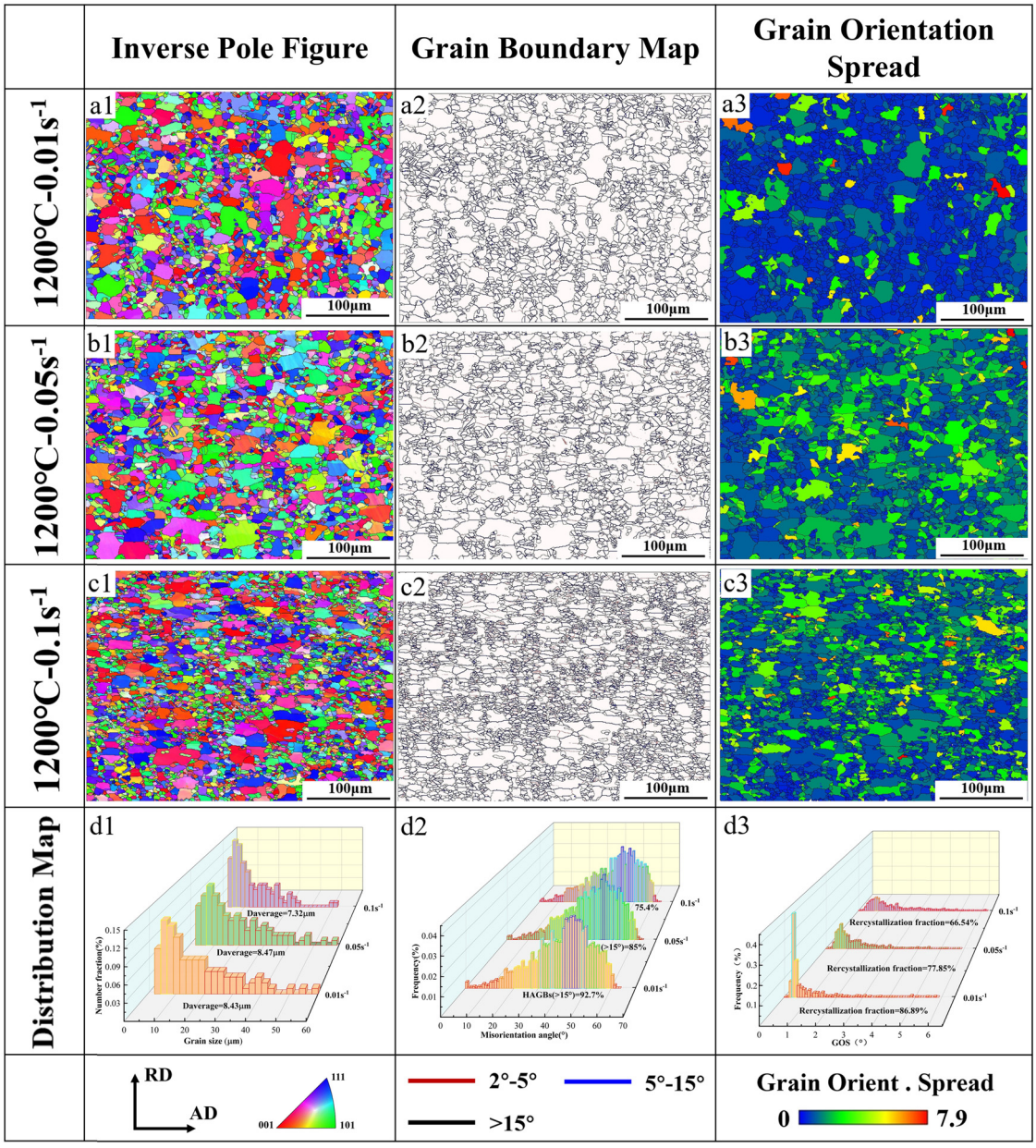

Figure 11: IPF maps, GB maps, and GOS maps of high-chromium cast steel at a deformation temperature of 1,200°C under different strain rates: (a1–a3) microscopic images at an strain rate of 0.01 s^{-1}, (b1–b3) microscopic images at a strain rate of 0.05 s^{-1}, (c1–c3) microscopic images at a strain rate of 0.1 s^{-1}, (d1–d3) average grain size distribution diagrams, high-angle grain boundary distribution diagrams and recrystallization distribution diagrams at strain rates ranging from 0.01 s^{-1} to 0.1 s^{-1}.

correspondingly increased peak flow stress. The grain refinement mechanism involves: the accelerated strain rates limit atomic diffusion, thereby inhibiting dislocation motion and recovery processes, and the reduced deformation times restrict energy absorption by fine grains and twins, ultimately producing a structure of fine equiaxed grains surrounding larger deformed grains. The most pronounced refinement occurred at 0.1 s^{-1}, coinciding with maximum flow stress [44], indicating that high strain rate influences microstructural evolution.

Figure 11(a2)–(d2) presents GB maps and GB distributions. The microstructure remains predominantly composed of HAGBs, though their fraction exhibits significant strain rate dependence. When the strain rate increases from 0.01 to 0.1 s^{-1} at 1,200°C, the HAGB proportion decreases substantially from 92.7 to 75.4%, with a reduction rate of 17.3%. LAGBs and MAGBs are randomly distributed around HAGBs, indicating that at high strain rates, fine grains can only transform into LAGBs and MAGBs due to insufficient energy supply. As deformation progresses, fine recrystallized grains are continuously formed within the material, absorbing the distortion energy stored in the microstructure. These grains further nucleate into recrystallized grains with HAGBs, which is consistent with the nucleation principles of DDRX [42]. Figure 11(a3)–(c3) displays GOS maps at 1,200°C and different strain rates. As the strain rate increases, there are deformed grains randomly distributed around recrystallized grains and also multiple slip bands. The reason is that severe deformation during thermal compression activated the dislocation slip mechanism within grains. At higher strain rates, a single slip system was insufficient to accommodate complex deformation between grains, so multiple slip characteristics were observed [45]. Figure 11(d3), The recrystallization rate demonstrates an inverse relationship with strain rate, decreasing from 86.89% at 0.01 s^{-1} to 66.54% at 0.1 s^{-1}. The reason is that the accumulation of deformation activation energy, dislocations near slip bands, and shorter deformation time are adverse to energy absorption by recrystallized grains. Since DRX is a slow nucleation process, insufficient energy absorption reduces the efficiency of recrystallization and nucleation. Additionally, to accommodate the overall deformation process, twins form in dislocation accumulation regions, absorbing activation energy nearby and further hindering recrystallization.

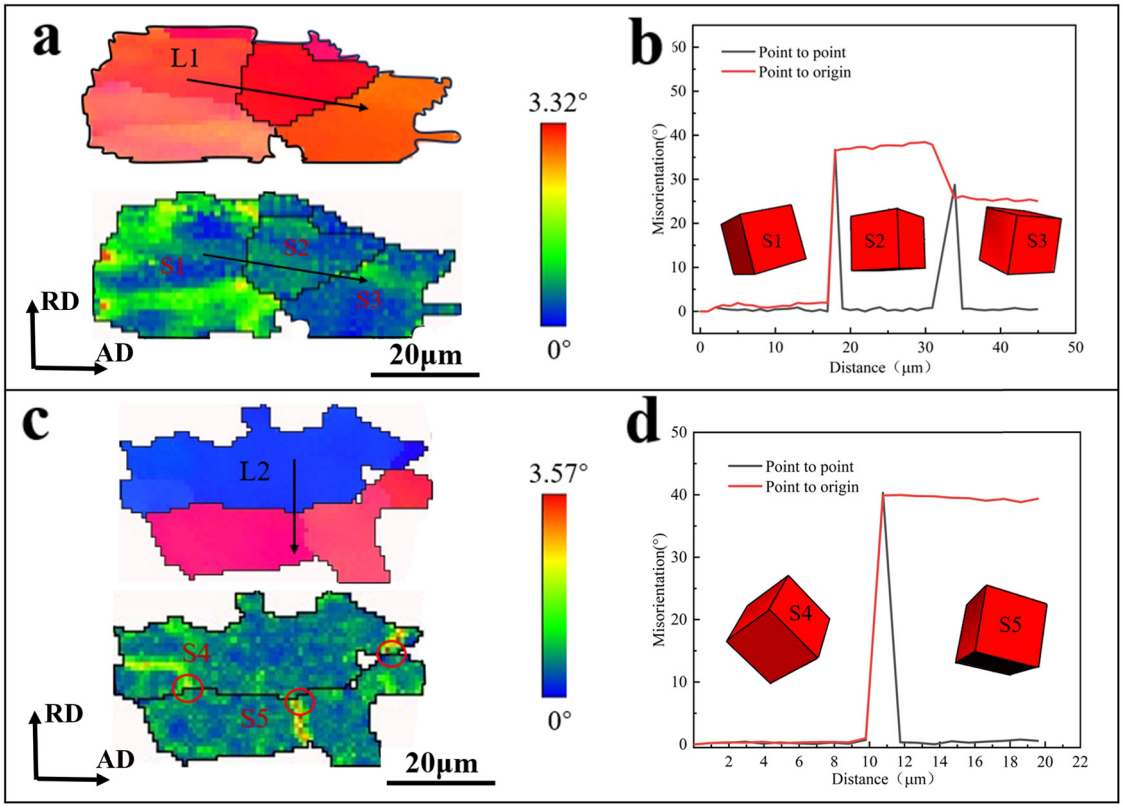

Figure 12: Local magnification of the microscopic grains of high-chromium cast steel at 1,200°C and strain rate 0.1 s^{-1}: (a) IPF image, (b) GND distribution image, (c) distribution of grain orientation difference along L1 direction, and (d) distribution of grain orientation difference along L2 direction.

The crystal orientation evolution and recrystallization nucleation mechanisms of grains in high-chromium cast steel were analyzed. Figure 12 presents a magnified internal view of grains and their orientation relationships in high-chromium cast steel at 1,200°C–0.1 s^{-1}. In Figure 12(a) and (b), line L1 passes through grains S1 (106.32°, 2.89°, 89.02°), S2 (261°, 31.79°, 13.37°), and S3 (71.53°, 37.09°, 14.04°). Based on cumulative misorientation measurements, the misorientation between S2 and S1 is 40°, while that between S3 and S1 is 25°. Compared with those in the standard orientation map, grains S1, S2, and S3 in the misorientation map exhibit a tendency to shift toward the < 001 > orientation. It indicates significant preferred orientation. On the geometrically necessary dislocation (GND) density map, the dislocation density in grain S1 is higher than that in grains S2 and S3. Dislocations in the S1 GB are transferring to adjacent boundaries (S2 and S3) through slipping and climbing, as indicated by the arrow along line L1. This phenomenon leads to the disappearance of some grain boundaries. As thermal deformation progresses, atomic diffusion and orientation adjustment between grains cause multiple grains to merge into a larger recrystallized grain with a consistent orientation. This finding reveals a typical subgrain merging nucleation mechanism [45]. In Figure 12(c) and (d), line L2 passes through grains S4 (335.77°, 40°, 64.74°) and S5 (121.07°, 24.93°, 47.79°), with a cumulative misorientation of 40° between them. The red lines highlight a GB "protrusion" phenomenon, which occurs because deformation during thermal compression is nonuniform, and the degree of grain deformation determines the dislocation density. To balance the uneven deformation between grains, the GB bulges toward the region with higher dislocation densities, and eventually low-dislocation-density and strain-free re-crystallized grains are formed. This result reveals a typical GB protrusion nucleation mechanism [46]. In summary, DDRX, primarily through subgrain merging and GB protrusion, is the dominant nucleation mechanism in high-chromium cast steel.

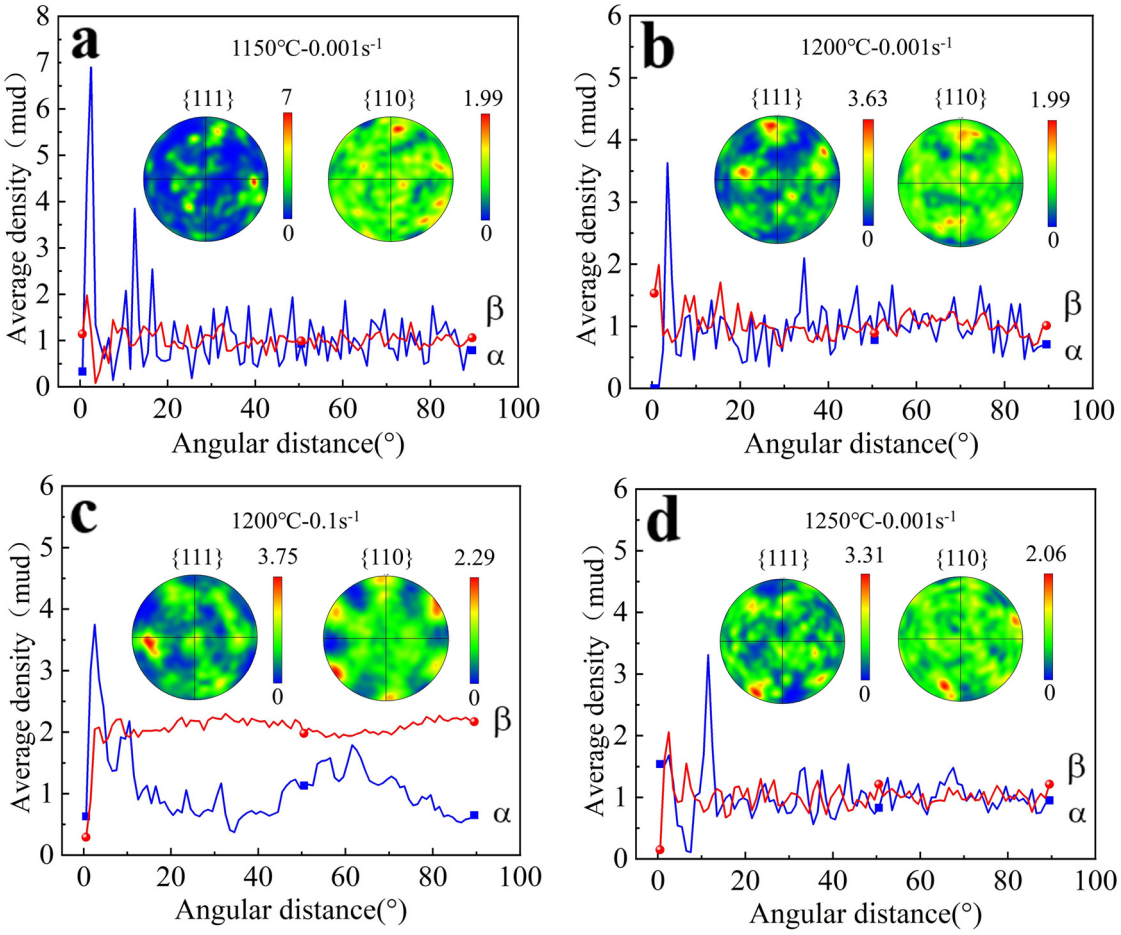

Figure 13: Pole diagram of *α* phase and *β* phase of high-chromium cast steel under different deformation conditions: (a) 1,150°C–0.001 s^{-1}, (b) 1,200°C–0.001 s^{-1}, (c) 1,200°C–0.1 s^{-1}, and (d) 1,250°C–0.001 s^{-1}.

3.4.4 Textile analysis

Figure 13 presents the polar diagrams of α and β phases in high-chromium cast steel under varying deformation conditions. Texture evolution analysis (Figure 13a, b and d) reveals that at a constant strain rate of 0.001 s^{-1}, the α phase exhibits progressive texture weakening with increasing deformation temperature. The average pole density decreases substantially from 7 mud at 1,150°C to 3.31 mud at 1,250°C, representing a 52.7% reduction in texture intensity. It indicates that the texture strength gradually weakened with the increasing deformation temperature. The reason is that, as the deformation temperature increased, high-chromium cast steel grains had sufficient energy for DRX, which promoted the random distribution of α phase orientations and reduced the strength of the deformation texture [47]. The average extreme density of the β phase increases from 1.99 mud to 2.06 mud. It is because multiple dislocation slip systems activated and twinning during thermal deformation acted jointly on the deformation process. As a result, the β phase underwent continuous rotations in a specific direction, and a stronger texture was formed.

As evidenced in Figure 13(b) and (c), isothermal deformation at 1,200°C reveals a distinct positive correlation between strain rate and texture strength for both α and β phases. Quantitative texture analysis shows that the α phase develops stronger textures than β phase across all strain rates, with their respective pole densities increasing from 3.63 mud (α) and 1.99 mud (β) at 0.001 s^{-1}. It is because a lower strain rate provides sufficient time for grains to fully absorb dislocation energy during thermal deformation, promoting DRX and the formation of more random orientation relationships. Ultimately, the texture strength is weaker. The polar diagrams exhibit an approximately symmetric hexagonal pattern at 0.1 s^{-1}, indicating that the grain orientation is closer to the original one under these conditions. The reason is that DRX has less effect on the texture strength, and most α and β phases retain their original orientation relationships, leading to relatively high texture strength.

4 Conclusion

(1) This work establishes an intrinsic model for the thermal deformation process of high-chromium cast steel: $\sigma = \frac{1}{\alpha}\ln\{\left(\frac{Z}{A}\right)^{\frac{1}{n}} + [\left(\frac{Z}{A}\right)^{\frac{2}{n}} + 1]^{\frac{1}{2}}\}$, determining the main parameters as follows:

$$\alpha = 0.05248 - 0.13546\varepsilon + 1.53978\varepsilon^2 - 5.68708\varepsilon^3 + 7.17332\varepsilon^4$$

$$n = 2.03541 + 5.77662\varepsilon - 43.5612\varepsilon^2 + 134.3812\varepsilon^3 - 157.588\varepsilon^4$$

$$Q = 334.35249 - 1060.75539\varepsilon + 12232.8385\varepsilon^2 - 45902.8302\varepsilon^3 + 53942.39428\varepsilon^4$$

$$\ln A = 23.19775 + 20.71486\varepsilon + 243.3865\varepsilon^2 - 1526.92\varepsilon^3 + 2036.609\varepsilon^4$$

The correlation coefficient R = 99.524 and AARE = 4.93% showed good reliability.

(2) Through analysis of three-dimensional power dissipation and instability maps, this study reveals a progressive expansion of the flow instability domain with increasing true strain during hot deformation of high-chromium cast steel. The constructed processing map at ε = 0.35 identifies an optimal safe processing window characterized by 1,190–1,240°C, 0.001–0.005 s^{-1}, where optimal workability is achieved.

(3) The high-chromium cast steel exhibited pronounced thermal sensitivity, where elevated deformation temperatures significantly enhanced dynamic softening effects. Microstructural evolution followed a characteristic parabolic trend, with average grain size initially decreasing before subsequent coarsening. Under optimal processing conditions (1,200°C–0.001 s^{-1}), the material exhibited partial CDRX, achieving simultaneous grain refinement (8.37 μm) and high recrystallization completeness (92.20%). This behavior suggests temperature-dependent competition between recrystallization nucleation and grain growth mechanisms.

(4) 1,200°C−0.1 s^{-1}, the grain undergoes severe deformation to stimulate the internal dislocation slip mechanism of the grain, and multiple slip features are observed, which ultimately determines that discontinuous DRX dominated by subgrain merging and GB protrusion is the main nucleation mechanism of high-chromium cast steel. The α phase-averaged density value decreases with increasing deformation temperature and decreasing strain rate, the β phase exhibits the opposite trend. These differential responses are principally governed by DRX mechanisms, where α-phase undergoes more complete recrystallization-induced texture randomization while β-phase retains deformation textures.

Acknowledgments: The authors sincerely thank the High-End Heavy Machinery Equipment Research Institute of Taiyuan University of Science and Technology and the

National Key Laboratory of Advanced Stainless Steel for their financial support. At the same time, we are grateful to the editors and the reviewers for their professional suggestions regarding the article.

Funding information: This work was supported by the National Natural Science Foundation of China (No. 52275357), the Scientific Research Initial Foundation of Taiyuan University of Science and Technology (No. 20232106, No. 20242076), and China International College Students Innovation Competition Excellence Program (PY20240118).

Author contributions: Songning Li: writing – original draft, methodology, and investigation. Peisheng Han: funding acquisition and conceptualization. Yunlin Xing: writing – review and editing and software. Yunlong Zhu: writing – review and editing and conceptualization. Xiaogang Wang: funding acquisition and conceptualization.

Conflict of interest: The authors state no conflict of interest.

Data availability statement: The data supporting our claims are available with the corresponding author and can be availed upon reasonable request.

References

[1] Zhang, Z., D. Delagnes, and G. Bernhart. Microstructure evolution of hot-work tool steels during tempering and definition of a kinetic law based on hardness measurements. *Materials Science and Engineering: A*, Vol. 380, No. 1–2, 2004, pp. 222–230.

[2] Zhang, S. J. and Y. F. Zhou. Research on high temperature oxidation resistance of a new austenitic heat resistant alloy. *Foundry*, Vol. 62, No. 12, 2013, pp. 1219–1222.

[3] Yang, H. F. Defect analysis and application of Heat-resistant cast Steel liner (ZG35Cr24Ni7SiN). *Science and Technology Information*, Vol. 5, 2011, id. 100+135.

[4] Lu, Q., W. Xu, and S. van der Zwaag. Designing new corrosion resistant ferritic heat resistant steel based on optimal solid solution strengthening and minimisation of undesirable microstructural components. *Computational Materials Science*, Vol. 84, 2014, pp. 198–205.

[5] Zhang, Y., C. H. Yao, Y. X. Tian, and B. Wang. China's coal industry accidents statistical analysis. *Journal of Mining Technology*, Vol. 24, No. 02, 2024, pp. 254–258.

[6] Calzavara-Pinton, P., J. Čelakovská, H. Lapeere, G. Holzer, M. Al-Ahmad, C. Y. Chu, et al. Multidimensional analysis of coal mine safety accidents in China–70 years review. *Mining, Metallurgy & Exploration*, Vol. 40, No. 1, 2023, pp. 253–262.

[7] Mehtonen, S. V., L. P. Karjalainen, and D. A. Porter. Hot deformation behavior and microstructure evolution of a stabilized high-Cr ferritic stainless steel. *Materials Science and Engineering: A*, Vol. 571, 2013, pp. 1–12.

[8] Lu, P. P. and W. Li. Influence of heat treatment process on the organization and hard toughness of wear-resistant and corrosion-resistant high-chromium alloy steel. *Thermal Processing Technology*, Vol. 41, No. 12, 2012, id. 3.

[9] Aly, B. M. Development of the hot forming system using reconfigurable forming dies, digital twin and topology optimisation [D]. *Brunel University*, London, 2021.

[10] Sun, Y., J. Li, Y. Sun, L. Song, Q. Yang, and X. Wang. Modeling and simulation of shape control based on digital twin technology in hot strip rolling. *Sensors*, Vol. 24, No. 2, 2024, id. 614.

[11] Ye, M. Y., J. C. Li, W. Quan, S. L. Li, and X. P. Du. Thermal compression constitutive equation and thermal working diagram of 06Cr23Ni13 stainless steel. *Journal of Materials, Heat Treatment*, No. 1, 2024, pp. 193–199 + 208.

[12] Chen, Y., H. Su, F. Zhao, J. Ye, B. Ouyang, Y. Wang, et al. Investigation of hot deformation behavior and microstructure evolution of TC18 alloy and establishment of constitutive equation under friction-temperature correction. *Materials Today Communications*, Vol. 39, 2024, id. 109075.

[13] Park, K. B., Y. T. Cho, and Y. G. Jung. Determination of Johnson-Cook constitutive equation for Inconel 601. *Journal of Mechanical Science and Technology*, Vol. 32, No. 4, 2018, pp. 1569–1574.

[14] Prasad, Y. V. R. K., H. L. Gegel, S. M. Doraivelu, J. C. Malas, J. T. Morgan, K. A. Lark, et al. Modeling of dynamic material behavior in hot deformation: Forging of Ti-6242. *Metallurgical Transactions A*, Vol. 15, 1984, pp. 1883–1892.

[15] Sun, Y., Z. Cao, Z. Wan, L. Hu, W. Ye, N. Li, et al. 3D processing map and hot deformation behavior of 6A02 aluminum alloy. *Journal of Alloys and Compounds*, Vol. 742, 2018, pp. 356–368.

[16] Wang M, Huang L, Chen M, Wang Y. Processing map and hot working mechanisms of Cu-Ag alloy in hot compression process. *Journal of Central South University*, Vol. 22, No. 3, 2015, pp. 821–828.

[17] Huang, K. E. and R. E. Logé. A review of dynamic recrystallization phenomena in metallic materials. *Materials & Design*, Vol. 111, 2016, pp. 548–574.

[18] Cizek, P. The microstructure evolution and softening processes during high-temperature deformation of a 21Cr–10Ni–3Mo duplex stainless steel. *Acta Materialia*, Vol. 106, 2016, pp. 129–143.

[19] Galiyev, A., R. Kaibyshev, and G. Gottstein. Correlation of plastic deformation and dynamic recrystallization in magnesium alloy ZK60. *Acta materialia*, Vol. 49, No. 7, 2001, pp. 1199–1207.

[20] Bruno, F., G. Konstantopoulos, G. Fiore, E. Rossi, M. Sebastiani, and C. Charitidis. A novel machine learning method to exploit EBSD and nanoindentation for TRIP steels microstructures analysis. *Materials & Design*, Vol. 239, 2024, id. 112774.

[21] Vilalta-Clemente, A., G. Naresh-Kumar, M. Nouf-Allehiani, P. Gamarra, M. A. di Forte-Poisson, C. Trager-Cowan, et al. Cross-correlation based high resolution electron backscatter diffraction and electron channelling contrast imaging for strain map and dislocation distributions in InAlN thin films. *Acta Materialia*, Vol. 125, 2017, pp. 125–135.

[22] Gussev, M. N., D. A. McClintock, T. S. Byun, and T. G. Lach. Recent progress in analysis of strain-induced phenomena in irradiated metallic materials and advanced alloys using SEM-EBSD in-situ tensile testing. *Current Opinion in Solid State and Materials Science*, Vol. 28, 2024, id. 101132.

[23] Saeidi, N., F. Ashrafizadeh, B. Niroumand, and F. Barlat. EBSD study of micromechanisms involved in high deformation ability of DP steels. *Materials & Design*, Vol. 87, 2015, pp. 130–137.

[24] Li, X., W. Xia, H. Yan, J. Chen, B. Su, M. Song, et al. High strength and large ductility of a fine-grained Al–Mg alloy processed by high strain rate hot rolling and cold rolling. *Materials Science and Engineering: A*, Vol. 787, 2020, id. 139481.
[25] Liu, J., J. Liu, X. Wang, C. Fu, Y. Wang, L. Lu, et al. Phase-transformation dynamics and characterization of precipitates in the Cu-3Ti-3ni-0.5 Si Alloy. *Materials and Technology*, Vol. 55, No. 4, 2021, pp. 483–489.
[26] Li, M. Y., Y. Wang, and B. Han. The kinetics of phase transformations during tempering in laser melted high chromium cast steel. *Journal of Materials Engineering and Performance*, Vol. 21, 2012, pp. 1091–1098.
[27] Li, Y. S., B. Han, and C. Gao. Microstructure Characteristic of Laser Cladding Ceramic Layer on High Cr Cast Steel Surface. *Advanced Materials Research*, Vol. 652, 2013, pp. 1866–1870.
[28] Cen, Q., H. Zhang, and H. Fu. Effect of heat treatment on structure and wear resistance of high chromium cast steel containing boron. *Journal of Iron and Steel Research International*, Vol. 21, No. 5, 2014, pp. 532–538.
[29] Razavinejad, R., S. Firoozi, and S. M. H. Mirbagheri. Effect of Titanium Addition on As Cast Structure and Macrosegregation of High-Carbon High-Chromium Steel. *Steel Research International*, Vol. 83, No. 9, 2012, pp. 861–869.
[30] Bialobrzeska, B., R. Jasiński, R. Dziurka, and P. Bała. Effect of chromium and titanium on the microstructure and mechanical properties of cast steel. Journal of Mining and Metallurgy. *Section B: Metallurgy*, Vol. 60, No. 2, 2024, pp. 235–257.
[31] Wang, G., Q. Wang, H. Che, Y. Li, and M. Lei. Effects of silicon on the microstructure and properties of cast duplex stainless steel with ultra-high chromium and high carbon. *Acta Metall Sin*, Vol. 56, No. 3, 2019, pp. 278–290.
[32] Li, D., Z. Zhu, S. Xiao, G. Zhang, and Y. Lu. Plastic flow behavior based on thermal activation and dynamic constitutive equation of 25CrMo4 steel during impact compression. *Materials Science and Engineering: A*, Vol. 707, 2017, pp. 459–465.
[33] Akbarzadeh, A. and S. Naghdy. Hot workability of a high carbon high chromium tool steel. *Materials & Design*, Vol. 2015, 2013, pp. 654–659.
[34] ASTM E209-18, Standard Practice for Compression Tests of Metallic Materials at Elevated Temperatures with Conventional or Rapid Heating Rates and Strain Rates[S].
[35] Li, J., R. An, S. Lai, L. Li, S. Liu, and H. Xu. Constitutive model over wide temperature range and considering negative-to-positive strain rate sensitivity for as-Quenched AA2219 sheet. *Journal of Materials Engineering and Performance*, Vol. 28, 2019, pp. 404–413.
[36] Xia, Y., X. Shu, Q. Zhang, Z. Pater, Z. Li, H. Xu, et al. Modified Arrhenius constitutive model and simulation verification of 2A12-T4 aluminum alloy during hot compression. *Journal of Materials Research and Technology*, Vol. 26, 2023, pp. 1325–1340.
[37] Wang, Z., W. Fu, B. Wang, W. Zhang, Z. Lv, and P. Jiang. Study on hot deformation characteristics of 12% Cr ultra-super-critical rotor steel using processing maps and Zener–Hollomon parameter. *Materials Characterization*, Vol. 61, No. 1, 2010, pp. 25–30.
[38] Fang, X. Q., J. B. Wang, S. Y. Liu, J. Z. Wen, H. Y. Song, and H. T. Liu. Microstructure evolution, hot deformation behavior and processing maps of an FeCrAl alloy. *Materials*, Vol. 17, No. 8, 2024, id. 1847.
[39] Mokdad, F., D. L. Chen, Z. Y. Liu, D. R. Ni, B. L. Xiao, and Z. Y. Ma. Three-dimensional processing maps and microstructural evolution of a CNT-reinforced Al-Cu-Mg nanocomposite. *Materials Science and Engineering: A*, Vol. 702, 2017, pp. 425–437.
[40] Wang, M., R. Wang, L. Meng, and G. Wang. Processing maps and hot working mechanisms of supercritical martensitic stainless steel. *Journal of Central South University*, Vol. 23, No. 7, 2016, pp. 1556–1563.
[41] Jiang, H., B. Yang, Y. Wu, B. Peng, and M. He. Deformation behaviors and microstructure evolution of Mg-Zn-Y-Zr Alloys during hot compression process. *Metals*, Vol. 14, No. 12, 2024, id. 1332.
[42] Wang, S. H., F. C. Li, Y. R. Xu, S. C. Wang. Inoculant addition amount of high carbon high chromium cast steel. *The Influence of Casting Technology*, Vol. 37, No. 3, 2016, pp. 514–516.
[43] Mirzadeh, H. Grain refinement of magnesium alloys by dynamic recrystallization (DRX): A review. *Journal of Materials Research and Technology*, Vol. 25, 2023, pp. 7050–7077.
[44] Gao, T., L. Liu, K. Zhao, S. Liu, M. Han, G. Liu, et al. Design and fabrication of a (6.4 γ–Al_2O_3 + 18$Al_{13}Fe_4$)/Al (wt%) composite utilizing fine grain strengthening and dispersion strengthening at elevated temperatures. *Materials & Design*, Vol. 215, 2022, id. 110432.
[45] Wang, Q., R. Zhou, Y. Li, and B. Geng. Characteristics of dynamic recrystallization in semi-solid CuSn10P1 alloy during hot deformation. *Materials Characterization*, Vol. 159, 2020, id. 109996.
[46] Bi, Y., B. Chen, L. Lu, J. Yang, X. Zhang, Z. Xu, et al. Hot-working characteristics and microstructure analysis of Zr-Sn alloy at different temperatures and strain rates. *Materials Today Communications*, Vol. 40, 2024, id. 109524.
[47] Li, L., J. Luo, J. J. Yan, and M. Q. Li. Dynamic globularization and restoration mechanism of Ti–5Al–2Sn–2Zr–4Mo–4Cr alloy during isothermal compression. *Journal of Alloys and Compounds*, Vol. 622, 2015, pp. 174–183.